

Constraining Sterile Neutrino Dark Matter in the Milky Way Halo with Swift-XRT

DOMINIC SICILIAN,¹ DANNELL LOPEZ,^{1,2} MASSIMO MOSCETTI,^{1,3,4} ESRA BULBUL,⁵ AND NICO CAPPELLUTI¹

¹*Department of Physics, University of Miami, Coral Gables, Florida 33146, USA*

²*School for Advanced Studies – Wolfson Campus, Miami, Florida 33132, USA*

³*Vanderbilt University, Nashville, Tennessee 37240, USA*

⁴*Palmer Trinity School, Miami, Florida 33157, USA*

⁵*Max Planck Institute for Extraterrestrial Physics, Garching bei München, Bayern, Germany*

ABSTRACT

We present a search for sterile neutrino dark matter decay signals in the Milky Way’s dark matter halo by considering the entirety of the Swift-XRT data archive. After filtering the raw archive, we analyze a ~ 77 Ms data set containing the full field of view, as well as a ~ 41 Ms data set with point-sources excised using the Swift-XRT Point Source catalog. We report non-detections of emission lines across the 3–6 keV continuum in both data sets, including at and around 3.5 keV. The point-sources excised data set is found to have higher sensitivity to faint dark matter decay signals due to its freedom from point-source contamination and is thus used to set constraints. Non-detections across the total data set’s continuum are used to constrain the sterile neutrino dark matter parameter space, marginally strengthening existing X-ray constraints. Non-detections at ~ 3.5 keV in data subsets grouped by angular distance from the galactic center are used to constrain the 3.5 keV line’s galactic intensity profile, providing the strongest constraints to date across $\sim 1/4$ of the galaxy.

1. INTRODUCTION

The sterile neutrino is a popular dark matter (DM) candidate, as it is a natural extension to the Standard Model and can be tested using current X-ray observatories (see, e.g., Dodelson & Widrow 1994; Abazajian et al. 2001a; Abazajian et al. 2001b; Laine & Shaposhnikov 2008; Boyarsky et al. 2019). This testability is due to the particle’s decay mechanism, dictated by the mixing angle $\sin^2(2\theta)$, which releases a photon with $E = m_{\nu_s}/2$ (where m_{ν_s} is the sterile neutrino mass; Pal & Wolfenstein 1982) and is therefore within X-ray bands for $m_{\nu_s} \sim 10$ keV.

Sterile neutrino DM garnered heavy attention when Bulbul et al. (2014) observed an unidentified emission line at ~ 3.5 keV in various galaxy clusters, found to be consistent with ~ 7 keV sterile neutrino decay. Afterwards, the 3.5 keV line was repeatedly detected in several DM-dominated objects such as clusters, M31, and the galactic center (GC) using multiple X-ray telescopes (Boyarsky et al. 2014; Wik et al. 2014; Boyarsky et al. 2015; Urban et al. 2015; Neronov et al. 2016a; Franse et al. 2016; Cappelluti et al. 2018; Hofmann & Wegg 2019). Other X-ray works did not detect unidentified emission

at 3.5 keV or any other energy, setting constraints on the $\sin^2(2\theta)$ vs. m_{ν_s} parameter space (Tamura et al. 2015; Ng et al. 2015; Bulbul et al. 2016; Ruchayskiy et al. 2016; Hitomi Collaboration et al. 2017; Perez et al. 2017; Dessert et al. 2020; Bhargava et al. 2020; Sicilian et al. 2020; Silich et al. 2021; Foster et al. 2021; Roach et al. 2022). In particular, the keV-mass parameter space has been most strongly constrained by works that used large-scale blank-sky data sets from major X-ray observatories including Chandra (Sicilian et al. 2020), XMM-Newton (Dessert et al. 2020; Foster et al. 2021), and NuSTAR (Neronov et al. 2016a; Roach et al. 2020; Roach et al. 2022), which make use of the ubiquitous, DM-dominated Milky Way Halo (MWH).

Here, we perform a similar MWH analysis using Swift-XRT, an instrument chosen for three reasons. First, its archive is vast and yet-untapped for MWH sterile neutrino constraints, and thus we sought to continue to push current technology to its limits by mining the archive of another major telescope. Secondly, it is important to test data from all X-ray observatories to test the instrumental origins of putative features such as the 3.5 keV line. And third, despite its relatively low grasp, Swift’s low-Earth orbit affords it a substantially lower and more stable non-X-ray particle background (NXB) than Chandra or XMM-Newton, potentially giving it improved sensitivity to a sterile neutrino DM signal in

the $m_{\nu_s} \sim 5\text{--}10$ keV range, where X-ray constraints have typically been dominated by Chandra and XMM-Newton.

In this work, we consider the entirety of the Swift-XRT data archive up to 2021. This unfiltered data set contains ~ 188 Ms of exposure time and, due to the short average exposure of Swift observations, consists of ~ 2 orders of magnitude more observations than Sicilian et al. (2020)’s ~ 51 Ms Chandra data set, thus giving nearly all-sky coverage. We hence aim to use Swift’s low NXB, the large data set, and its wide spatial distribution to constrain both the sterile neutrino DM parameter space and the galactic intensity profile of the 3.5 keV line. Our methodology closely follows that of Sicilian et al. (2020), which is thoroughly described in that work and summarized here.

2. DATA SELECTION AND REDUCTION

To minimize contamination from extended sources, we excluded observations pointed through the galactic plane ($|b| \leq 10^\circ$) or within 2° of major known extended sources, including the Crab Nebula and any object in either the ROSAT galaxy cluster catalog (ROSGALCLUS; Vikhlinin et al. 1998) or Chandra supernova remnant catalog¹. After applying these filters, the data set contained ~ 77 Ms of exposure time.

Upon applying standard Swift-XRT data reduction procedures², we replicated Moretti et al. (2009)’s methodology to extract both field of view (FOV) and NXB spectra from individual observations. In particular, the NXB was extracted from regions of the CCD not exposed during observations, while the FOV spectrum was taken from Moretti et al. (2009)’s conservatively-defined central ~ 0.054 deg² region to avoid contamination from out-of-time-event calibration.

To produce a data set with minimal point-source contamination, for any observation considered by the Swift-XRT Point Source catalog (2SXPS; Evans et al. 2020), we excised all documented sources in that observation according to the catalog-supplied point-spread function (PSF) at each source position. These point-sources excised (PSE) observations form a ~ 41 Ms data subset. This process was not as efficient as Sicilian et al. (2020)’s, since Chandra’s PSF is superior to Swift’s, but the much-lower continuum in the PSE compared to FOV shows we removed considerable contamination regardless. Excising point-sources inadvertently removes DM along the line-of-sight (LOS), and the lack of coverage offered by 2SXPS reduced our total exposure time by

nearly 50%, so therefore, like Sicilian et al. (2020), we analyzed both the ~ 41 Ms PSE and the full ~ 77 Ms FOV data sets.

We then binned the total PSE and FOV data sets by angular distance from the galactic center (θ_{GC}) to study the 3.5 keV line’s intensity profile as it compares to Navarro-Frenk-White (NFW; Navarro et al. 1997) predictions and prior measurements. Bins were determined by emulating Sicilian et al. (2020)’s estimation of the minimum Chandra exposure time needed to detect the 3.5 keV line as a function of θ_{GC} , which we modified to accommodate Swift. Sicilian et al. (2020)’s line profile constraints, while strong, were difficult to interpret near the GC, where NFW slope is steep, as that work was grouped into only 4 bins, with the innermost bin spanning $10\text{--}74^\circ$. Therefore, although Swift’s lower NXB relative to Chandra’s already relaxes bin exposure thresholds, we further amplified this by binning the data sets based on their exposure time after removing the galactic plane but before removing any other observations with extended sources, rather than their fully-filtered exposures. As a result, we may have sacrificed some strength in our profile constraints, but we were nonetheless able to greatly improve θ_{GC} resolution, with the PSE and FOV data sets yielding 9 and 13 bins, respectively.

Spectra were stacked using `mathpha` (from `FTOOLS`) to produce master FOV, PSE, and NXB spectra, as well as to produce the corresponding sets of θ_{GC} -binned spectra. Exposure-weighted response files were combined using `FTOOLS` `addrmf` and `addarf`. NXB spectra were renormalized to match each respective data set’s total counts in channels ≥ 725 , based on NXB-to-total spectral counts ratios computed in Moretti et al. (2009).

3. SPECTRAL ANALYSIS

Spectra were modeled using `PyXspec` (`XSPEC` 12.12.0) on the interval 3.0–6.0 keV, chosen to include 3.5 keV while avoiding known emission features (Moretti et al. 2009) and soft galactic diffuse emission, as well as giving more coverage than Sicilian et al. (2020). As shown in Moretti et al. (2009), the total blank-sky continuum in this band consists of $\sim 34\%$ cosmic X-ray background (CXB), $\sim 16\%$ off-axis stray-light (SL) due to Swift’s lack of Chandra/XMM-like baffles, and $\sim 51\%$ NXB. Spectra for the total PSE and FOV data sets are plotted in Figure 1 along with best-fit models produced through the procedure described below.

The astrophysical continuum was modeled using a broken power law folded through both the ARF and RMF which, like Moretti et al. (2009)’s CXB power law, is unabsorbed due to the low N_H across fields considered (Dickey & Lockman 1990) and its resulting lack of ab-

¹ <https://hea-www.harvard.edu/ChandraSNR/>

² https://swift.gsfc.nasa.gov/analysis/xrt_swguide.v1.2.pdf

	FOV	PSE
Γ_1	$1.84^{+0.04}_{-0.04}$	$2.70^{+0.19}_{-0.20}$
E_b (keV)	$3.98^{+0.07}_{-0.07}$	$3.96^{+0.11}_{-0.10}$
Γ_2	$1.21^{+0.05}_{-0.05}$	$-0.10^{+0.28}_{-0.24}$
$\log K$	$-3.30^{+0.02}_{-0.02}$	$-3.85^{+0.10}_{-0.11}$
$\Gamma_{1,\text{NXB}}$	$0.66^{+0.09}_{-0.09}$	$0.64^{+0.07}_{-0.08}$
$E_{b,\text{NXB}}$ (keV)	$5.31^{+0.09}_{-0.12}$	$5.23^{+0.12}_{-0.14}$
$\Gamma_{2,\text{NXB}}$	$-0.62^{+0.22}_{-0.21}$	$-0.38^{+0.19}_{-0.23}$
$\log K_{\text{NXB}}$	$-2.36^{+0.05}_{-0.06}$	$-2.45^{+0.05}_{-0.05}$
χ^2_ν	1.148	1.055

Table 1. Model parameter best-fit and 1σ error values from MCMC posteriors for the total PSE and FOV data sets. χ^2_ν is also reported to indicate goodness-of-fit. The top panel shows astrophysical parameters while the bottom shows NXB values. Γ represents photon indices, E_b is the break energy, and K indicates broken power law normalizations.

sorption in our model’s energy band. The NXB model was a broken power law folded only through the RMF, as the NXB arises strictly from particles that do not pass through Swift-XRT’s mirrors (Pagani et al. 2007; Bulbul et al. 2020). Visual inspection of the spectra revealed possible emission features at ~ 3.75 and ~ 5.88 keV, and our band also includes energies of known features at 3.3 and 3.68 keV modeled in Sicilian et al. (2020) whose origins—whether astrophysical or instrumental—are unclear. However, we can conclude from preliminary CSTAT (Cash 1979) optimization fits that, for both the FOV and PSE data sets, there are no significant features at these energies in either the astrophysical or NXB spectra, as we found ΔBIC -obtained significances approaching zero for those features, while no $\Delta\chi^2$ -computed significance exceeded $\sim 2\sigma$. These results were consistent regardless of whether line width was fixed or left free. Therefore, we do not include any such features in our final models.

Best-fit values for the reported models (Table 1) were obtained using Goodman-Weare MCMC fitting (with CSTAT as the fit statistic) to generate posterior parameter distributions. The resulting best-fit models for the total FOV and PSE spectra have reduced χ^2 (χ^2_ν) of ~ 1.1 , and all θ_{GC} -binned models have $\chi^2_\nu \sim 1.1$ – 1.2 , indicating the models are good fits.

3.1. The 3.5 keV Line

For sterile neutrino constraints, we first focused on the known 3.5 keV feature following Sicilian et al. (2020)’s procedure. We added an emission line with E free to vary from 3.4–3.6 keV, with width fixed at zero and thus

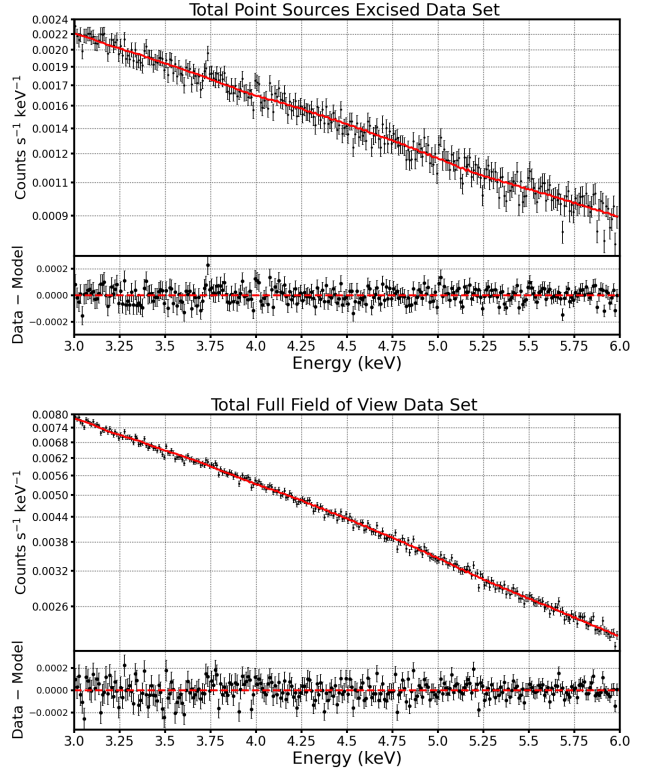


Figure 1. Spectra and best-fit models for the total PSE (top) and FOV (bottom) data sets.

dictated by the instrument response, then performed another MCMC fit, the posteriors of which revealed that E is generally poorly-constrained, with no convergence in the FOV line E posterior and mild convergence in PSE line E . Both had the same best-fit $E = 3.48$ keV and similar best-fit line fluxes $\log F_{\text{line}} \sim -8$. We isolated a feature with frozen $E = 3.48$ keV and performed an MCMC fit (with walkers initialized for $\log F_{\text{line}}$ between -8 and -7 to match the E -free best-fit F_{line} ’s order of magnitude, then left free to vary across all values). Using the resulting best-fit F_{line} , we assessed the significance of the feature using both $\Delta\chi^2$ and ΔBIC , finding it to approach zero for the total FOV and PSE models. The same results were found when repeating the procedure with Sicilian et al. (2020)’s frozen $E = 3.51$ keV. We therefore conclude that this is a non-detection of the 3.5 keV line.

We applied this method to all θ_{GC} bins in both the FOV and PSE data sets, adopting $E = 3.51$ keV for our frozen line E as in Sicilian et al. (2020), due to its use in that work, consistency with past detection energies, and proximity to the center of the allowed interval when we left line E free to vary due to the sporadic, inconsistent shapes and nature of convergences of the resulting E posterior distributions. The 3.51 keV fea-

ture yielded near-zero ΔBIC -computed significances for all θ_{GC} bins in both the PSE and FOV data sets and near-zero $\Delta\chi^2$ significances in all PSE bins, as well as in nearly all FOV bins, with no FOV bin exceeding $\sim 1\sigma$. These results thus further confirm our conclusion that we did not detect a 3.5 keV line.

3.2. The Continuum

To search for faint emission lines at other model energies, we performed the same process above across the remainder of the continuum. From 3–6 keV, we increased the frozen line E in steps of 50 eV (chosen to be smaller than Swift’s energy resolution and hence protect against skipping over a genuine feature) and used the MCMC-computed best-fit F_{line} to evaluate significance. In Figure 2, we have plotted line significance computed using ΔBIC and $\Delta\chi^2$ at all energies in both the FOV and PSE data sets. As shown, all ΔBIC -obtained significances were $\ll 1\sigma$. For nearly all energies in both models, $\Delta\chi^2$ significance was also $\ll 1\sigma$, and in all remaining cases was $< 2\sigma$. Therefore, we conclude that we did not detect any emission features consistent with sterile neutrino DM.

The 3σ upper-limit on the line flux at each energy is computed as the 0.997 quantile from that energy’s F_{line} MCMC posterior distribution, representing the 99.7% confidence interval above $F_{\text{line}} = 0$. We computed these limits for both the total FOV and PSE data sets, providing two sets of flux upper-limits at all energies considered across the continuum, including 3.48 and 3.51 keV. This method was also used to set upper-limits on the θ_{GC} 3.5 keV line flux for the 9 PSE bins and 13 FOV bins.

We compared our continuum constraints to a series of simulations to ensure the robustness of our upper-limit calculations, particularly to verify that the limits are not misleadingly low, which could conceivably occur if the MCMC walkers reach low F_{line} values early in the fit and remain localized throughout. The simulation procedure follows that of Sicilian et al. (2020), which repeatedly simulated an emission feature at each energy to compute the maximum F_{line} value that would have yielded a $\Delta\chi^2$ significance $< 3\sigma$ and hence managed to avoid detection. We computed these constraints for both the FOV and PSE spectra, then compared them to those obtained using MCMC. In both cases, the upper-limits generated by the simulations were more aggressive than the MCMC constraints by $\sim 24\%$, decisively confirming the validity of our results. Thus, we can now use our line flux upper-limits to constrain the 3.5 keV line’s θ_{GC} profile and compute sterile neutrino parameter space constraints.

4. RESULTS AND DISCUSSION

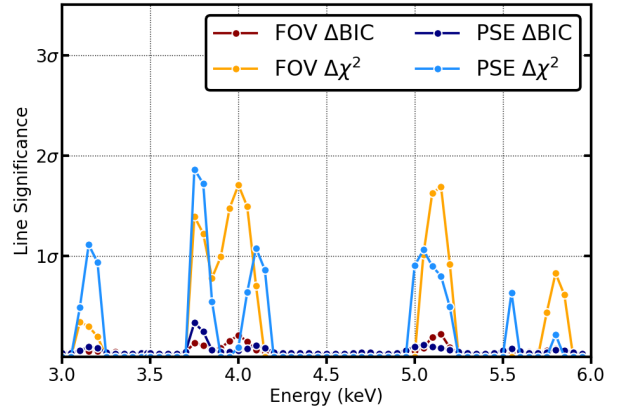


Figure 2. Data points indicate line significances when fitted at the discrete energies analyzed across the continuum. Connecting lines are used to enhance visualization.

Despite the FOV’s exposure time advantage and PSE’s loss of DM along the LOS due to point-source removal, the PSE’s line flux upper-limits for energies across the continuum are $\sim 17\%$ lower on average than the FOV’s flux limits, and its θ_{GC} bins yield $\sim 29\%$ more stringent profile constraints than those of the FOV. This is due to the higher sensitivity afforded to the PSE data by eliminating baryonic contamination from point sources and therefore minimizing continuum flux. For a faint DM signal, even when accounting for PSE’s LOS losses, we estimate the PSE’s signal-to-noise ratio (S/N) to be $\sim 22\%$ greater than that of the FOV data. It follows that the PSE data set should yield similarly more stringent constraints, which is highly consistent with our results. Therefore, like Sicilian et al. (2020), we have chosen to employ the PSE data set to determine DM constraints.

4.1. 3.5 keV Line Intensity Profile Constraints

Using our 3.5 keV line flux upper-limits in the θ_{GC} bins, we have computed and plotted the intensity upper-limit profile. Existing constraints and prior detections are shown in Figure 3, with the exception of Neronov et al. (2016a)’s NuSTAR detections, as their decaying DM origins were ruled out by Sicilian et al. (2020)’s profile constraints. Two example NFW-predicted profiles are shown for reference, computed by Cappelluti et al. (2018) and Boyarsky et al. (2018) based on different sets of NFW parameters and normalized by Boyarsky et al. (2015)’s GC detection. As shown in Figure 3, our constraints on the intensity profile are the strongest to date across $\sim 1/4$ of the galaxy, producing the most stringent limits in the regions $71\text{--}93^\circ$ and $117\text{--}147^\circ$, with Sicilian

et al. (2020)’s generally remaining the lowest everywhere else $\geq 10^\circ$.

As also illustrated by Figure 3, the higher θ_{GC} resolution relative to Sicilian et al. (2020) allows a more useful interpretation near the GC than the stronger Sicilian et al. (2020) upper-limit. Similarly, the Dessert et al. (2020) XMM MWH constraint (shown here with Sicilian et al. 2020’s adjustment based on Abazajian 2020, Boyarsky et al. 2020, and Dessert et al. 2020a) is nearly identical to Sicilian et al. (2020)’s in that region, but has $\sim 1/2$ the Swift constraints’ θ_{GC} resolution. The Swift constraints improve upon Silich et al. (2021)’s HaloSat limits with our 10–30° bin’s combination of strength and resolution relative to those of Silich et al. (2021)’s results.

However, by the same token, the Dessert et al. (2020) constraint may be more informative than ours in that region and appears inconsistent with the decaying DM origin of Boyarsky et al. (2018)’s detections between 10–35°, though there has been extensive discussion (Abazajian 2020; Boyarsky et al. 2020; Dessert et al. 2020a) challenging that limit due to concerns over Dessert et al. (2020)’s exclusion of 3.3 and 3.68 keV features in the final model, which heavily impacted that work’s constraints. Notably, we also excluded those features as they were not detected (Section 3), but ensured the robustness of our results by recomputing ~ 3.5 keV constraints when including 3.3 and 3.68 keV features in the total PSE model, finding that the line flux upper-limit differed by just $\sim 2\%$ at 3.51 keV and by less than 1%, on average, across the 3–4 keV band. Moreover, interestingly, the Boyarsky et al. (2018) detections are entirely consistent with our profile constraints.

4.2. Parameter Space Constraints

Due to the direct proportionality between $\sin^2(2\theta)$ and the sterile neutrino decay rate for a given m_{ν_s} , namely

$$\Gamma_\gamma(m_{\nu_s}, \theta) = 1.38 \times 10^{-29} \text{ s}^{-1} \frac{\sin^2(2\theta)}{10^{-7}} \left(\frac{m_{\nu_s}}{1 \text{ keV}} \right)^5, \quad (1)$$

where $\Gamma_\gamma(m_{\nu_s}, \theta)$ is the decay rate (Pal & Wolfenstein 1982), and the predicted flux of decaying DM emission (F_{DM}) from a given mass of DM in the FOV ($M_{DM,FOV}$) a distance D from the detector, given by

$$F_{DM} = \frac{\Gamma_\gamma}{4\pi m_{\nu_s}} \frac{M_{DM,FOV}}{D^2} \quad (2)$$

(Neronov & Malyshev 2016b), determining $\sin^2(2\theta)$ constraints from line flux upper-limits is dependent on the distribution of DM observed within the data set. The constraints, then, must be obtained by integrating the

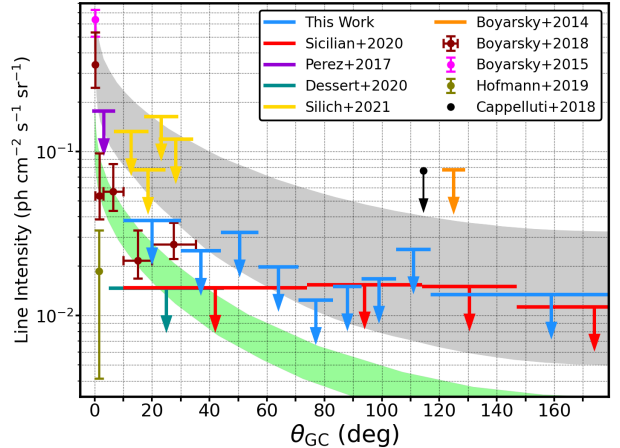


Figure 3. The Swift line intensity upper-limit profile plotted alongside existing constraints, prior detections, and two example NFW-predicted profiles for reference. The gray profile was computed by Cappelluti et al. (2018) (using Nesti & Salucci 2013’s parameters) while the green profile was computed by Boyarsky et al. (2018) (using McMillan 2017’s parameters). Shaded regions for both represent 2σ uncertainty ranges. Adapted from Sicilian et al. (2020).

DM density profile over the LOS and FOV and are therefore model-dependent on the profile function and its parameter values. As in Sicilian et al. (2020), when computing the continuum constraints, we performed the calculation twice—first using fairly aggressive NFW parameters based on the empirical Nesti & Salucci (2013) values (scale radius $R_s \sim 16$ kpc; local DM density ~ 0.67 GeV cm^{-3}) and again using conservative parameters detailed in Abazajian (2020) ($R_s = 26$ kpc; $\rho_\odot \sim 0.28$ GeV cm^{-3}).

The resulting Swift constraints on $\sin^2(2\theta)$ are plotted in Figure 4 along with other existing limits on the parameter space. Like Sicilian et al. (2020), we expect the true constraint to lie somewhere between the bounds generated by the different NFW parameter choices, so we have plotted the conservative curve as a dashed line, separated from the more aggressive curve by a translucent uncertainty region. As mentioned when computing continuum line flux upper-limits, unlike in Sicilian et al. (2020) these constraints were designed to include coverage for the 3.5 keV line, eliminating the need for a separate point on the plot.

As Figure 4 shows, despite the Swift exposure being $\sim 20\%$ less than Sicilian et al. (2020)’s ~ 51 Ms of Chandra exposure, the constraints are highly consistent and in fact our Swift constraints are slightly stronger overall, with the conservative limits $\sim 4\%$ more stringent than the conservative Chandra constraints and the

aggressive limits $\sim 1\%$ more stringent than the aggressive Chandra constraints. Notably, at $m_{\nu_s} \sim 7$ keV, our conservative constraints are just outside the collective 1σ error range of the Bulbul et al. (2014), Boyarsky et al. (2014), and Boyarsky et al. (2015) detections, providing evidence against the 3.5 keV line’s decaying DM interpretation. However, even our aggressive constraints remain consistent with Hofmann & Wegg (2019)’s detection, which means our results do not entirely eliminate the 3.5 keV line’s decaying DM interpretation, though Foster et al. (2021)’s results (which are stronger than ours at $m_{\nu_s} \sim 7$ keV) are outside even the Hofmann & Wegg (2019) 1σ error range. The overall DM origin of the 3.5 keV line also remains feasible in frameworks besides the sterile neutrino that may be observed in clusters but not galaxies (e.g., Cline et al. 2014; Cline & Frey 2014a; Cline & Frey 2014b; Finkbeiner & Weiner 2016). While the Foster et al. (2021)’s XMM MWH constraints are also more stringent overall than ours, towards the aggressive end of our limits we were able to match the XMM-Newton constraints at several m_{ν_s} values and improve upon XMM-Newton’s around ~ 6.7 and ~ 12 keV.

Therefore, the edge of the overall X-ray limits is now formed by constraints from Swift in this work, XMM in Foster et al. (2021), and NuSTAR in a combination of Neronov et al. (2016a), Perez et al. (2017), Ng et al. (2019), Roach et al. (2020), and Roach et al. (2022). Together, these X-ray constraints have eliminated most of the parameter space that remains above the big bang nucleosynthesis (BBN) lower limits, which are theoretical limits based on lepton asymmetry in the early Universe (see Dolgov et al. 2002; Serpico & Raffelt 2005; Laine & Shaposhnikov 2008; Boyarsky et al. 2009; Venumadhav et al. 2016; Roach et al. 2020). According to Dekker et al. (2021b), this small remainder of the parameter has been ruled out nearly entirely up to $m_{\nu_s} \sim 20$ keV based on that work’s study of small-scale structure formation around the MWH, though those results are dependent on systematics such as MWH mass, NFW parameters, and the extended Press-Schechter formalism (EPS; Schneider 2015; Cherry & Horiuchi 2017).

4.3. Closing Thoughts

We have found no evidence of sterile neutrino DM in the Swift-XRT MWH observations, and have used our non-detections to constrain the 3.5 keV line’s galactic intensity profile, as well as the sterile neutrino DM $\sin^2(2\theta)$ vs. m_{ν_s} parameter space. Our 3.5 keV line profile upper-limits are the strongest to date across $\sim 1/4$ of the galaxy and our parameter space limits marginally improve upon existing X-ray constraints. Swift has now

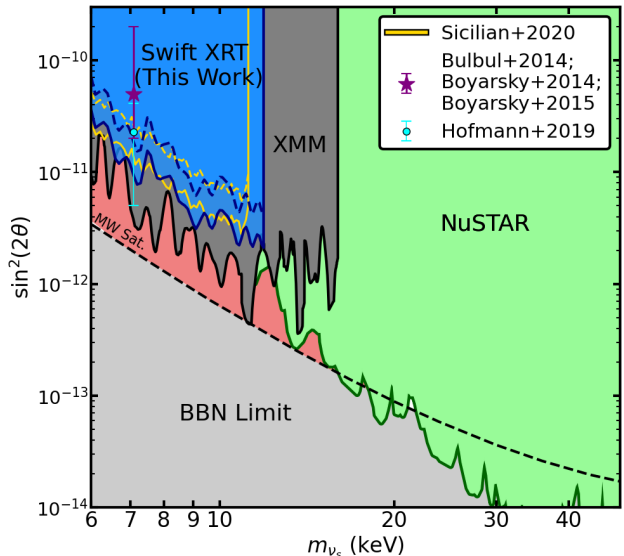


Figure 4. Constraints on the $\sin^2(2\theta)$ vs. m_{ν_s} parameter space. The red “MW Sat.” region represents Dekker et al. (2021b)’s study of small-scale structure, the dark gray “XMM” region indicates Foster et al. (2021), and the green “NuSTAR” region represents Neronov et al. (2016a), Perez et al. (2017), Ng et al. (2019), Roach et al. (2020), and Roach et al. (2022). Dashed gold represents the conservative Sicilian et al. (2020) Chandra constraint, while solid gold is the more aggressive constraint, with the gap between them representing NFW uncertainty. As described in the text, our Swift constraints are plotted in a similar way, with the uncertainty region appearing translucent while the region above the dashed conservative limit is solid. Purple and cyan data points show notable ~ 3.5 keV line detections. Adapted from Ng et al. (2019), Roach et al. (2020), and Sicilian et al. (2020).

joined Chandra, XMM-Newton, and NuSTAR on the list of major X-ray observatories whose vast archives have been harnessed in the search for decaying DM emission lines in the MWH. Since the constraints obtained from these observatories are fairly consistent, it appears we have collectively pushed existing technology and data to their limits, suggesting recent or future X-ray missions such as XRISM will be necessary to resolve lingering uncertainty on this topic. This sentiment is evidenced by Dekker et al. (2021a)’s simulations indicating eROSITA will achieve the required sensitivity to do so. Until then, the door will remain nearly closed, yet undeniably ajar, on sterile neutrino dark matter.

ACKNOWLEDGMENTS

DS kindly acknowledges NASA Swift Grant 80NSSC21K 1410 and the University of Miami for providing funding during the completion of this work. The authors thank the University of Miami Young Scholars Program for facilitating the contributions of future scientists to works such as this.

Software: Astropy (Astropy Collaboration et al. 2013; Astropy Collaboration et al. 2018), corner

(Foreman-Mackey 2016), HEASoft 6.29 (NASA High Energy Astrophysics Science Archive Research Center HEASARC), Matplotlib (Hunter 2007), NumPy (van der Walt et al. 2011), pandas (McKinney 2010; The pandas development team 2020), PyXspec (Arnaud 2016), Scikit-learn (Pedregosa et al. 2012), XSPEC 12.12.0 (Arnaud 1996)

REFERENCES

- Abazajian, K., Fuller, G. M., & Patel, M. 2001, *PhRvD*, 64, 023501. doi:10.1103/PhysRevD.64.023501
- Abazajian, K., Fuller, G. M., & Tucker, W. H. 2001, *ApJ*, 562, 593. doi:10.1086/323867
- Abazajian, K. N. 2020, arXiv:2004.06170
- Arnaud, K. A. 1996, *Astronomical Data Analysis Software and Systems V*, 101, 17
- Arnaud, K. A. 2016, *AAS/High Energy Astrophysics Division #15*
- Astropy Collaboration, Robitaille, T. P., Tollerud, E. J., et al. 2013, *A&A*, 558, A33. doi:10.1051/0004-6361/201322068
- Astropy Collaboration, Price-Whelan, A. M., Sipőcz, B. M., et al. 2018, *AJ*, 156, 123. doi:10.3847/1538-3881/aabc4f
- Bhargava, S., Giles, P. A., Romer, A. K., et al. 2020, *MNRAS*, 497, 656. doi:10.1093/mnras/staa1829
- Boyarsky, A., Ruchayskiy, O., & Shaposhnikov, M. 2009, *Annual Review of Nuclear and Particle Science*, 59, 191. doi:10.1146/annurev.nucl.010909.083654
- Boyarsky, A., Ruchayskiy, O., Iakubovskiy, D., et al. 2014, *PhRvL*, 113, 251301. doi:10.1103/PhysRevLett.113.251301
- Boyarsky, A., Franse, J., Iakubovskiy, D., et al. 2015, *PhRvL*, 115, 161301. doi:10.1103/PhysRevLett.115.161301
- Boyarsky, A., Iakubovskiy, D., Ruchayskiy, O., et al. 2018, arXiv:1812.10488
- Boyarsky, A., Drewes, M., Lasserre, T., et al. 2019, *Progress in Particle and Nuclear Physics*, 104, 1. doi:10.1016/j.pnnp.2018.07.004
- Boyarsky, A., Malyshev, D., Ruchayskiy, O., et al. 2020, arXiv:2004.06601
- Bulbul, E., Markevitch, M., Foster, A., et al. 2014, *ApJ*, 789, 13. doi:10.1088/0004-637X/789/1/13
- Bulbul, E., Markevitch, M., Foster, A., et al. 2016, *ApJ*, 831, 55. doi:10.3847/0004-637X/831/1/55
- Bulbul, E., Kraft, R., Nulsen, P., et al. 2020, *ApJ*, 891, 13. doi:10.3847/1538-4357/ab698a
- Cappelluti, N., Bulbul, E., Foster, A., et al. 2018, *ApJ*, 854, 179. doi:10.3847/1538-4357/aaa68
- Cash, W. 1979, *ApJ*, 228, 939. doi:10.1086/156922
- Cherry, J. F. & Horiuchi, S. 2017, *PhRvD*, 95, 083015. doi:10.1103/PhysRevD.95.083015
- Cline, J. M., Liu, Z., Moore, G. D., et al. 2014, *PhRvD*, 89, 121302. doi:10.1103/PhysRevD.89.121302
- Cline, J. M. & Frey, A. R. 2014, *JCAP*, 2014, 013. doi:10.1088/1475-7516/2014/10/013
- Cline, J. M. & Frey, A. R. 2014, *PhRvD*, 90, 123537. doi:10.1103/PhysRevD.90.123537
- Dekker, A., Peerbooms, E., Zimmer, F., et al. 2021, *PhRvD*, 104, 023021. doi:10.1103/PhysRevD.104.023021
- Dekker, A., Ando, S., Correa, C. A., et al. 2021, arXiv:2111.13137
- Dessert, C., Rodd, N. L., & Safdi, B. R. 2020, *Science*, 367, 1465. doi:10.1126/science.aaw3772
- Dessert, C., Rodd, N. L., & Safdi, B. R. 2020, *Physics of the Dark Universe*, 30, 100656. doi:10.1016/j.dark.2020.100656
- Dickey, J. M. & Lockman, F. J. 1990, *ARA&A*, 28, 215. doi:10.1146/annurev.aa.28.090190.001243
- Dolgov, A. D., Hansen, S. H., Pastor, S., et al. 2002, *Nuclear Physics B*, 632, 363. doi:10.1016/S0550-3213(02)00274-2
- Dodelson, S. & Widrow, L. M. 1994, *PhRvL*, 72, 17. doi:10.1103/PhysRevLett.72.17
- Evans, P. A., Page, K. L., Osborne, J. P., et al. 2020, *ApJS*, 247, 54. doi:10.3847/1538-4365/ab7db9
- Finkbeiner, D. P. & Weiner, N. 2016, *PhRvD*, 94, 083002. doi:10.1103/PhysRevD.94.083002
- Franse, J., Bulbul, E., Foster, A., et al. 2016, *ApJ*, 829, 124. doi:10.3847/0004-637X/829/2/124
- Foreman-Mackey, D. 2016, *The Journal of Open Source Software*, 1, 24. doi:10.21105/joss.00024

- Foster, J. W., Kongsore, M., Dessert, C., et al. 2021, *PhRvL*, 127, 051101.
doi:10.1103/PhysRevLett.127.051101
- Hitomi Collaboration, Aharonian, F., Akamatsu, H., et al. 2017, *Nature*, 551, 478. doi:10.1038/nature24301
- Hofmann, F. & Wegg, C. 2019, *A&A*, 625, L7.
doi:10.1051/0004-6361/201935561
- Hunter, J. D. 2007, *Computing in Science and Engineering*, 9, 90. doi:10.1109/MCSE.2007.55
- Laine, M. & Shaposhnikov, M. 2008, *JCAP*, 2008, 031.
doi:10.1088/1475-7516/2008/06/031
- McKinney, W. 2010, *Proceedings of the 9th Python in Science Conference*, 56.
doi:10.25080/Majora-92bf1922-00a
- McMillan, P. J. 2017, *MNRAS*, 465, 76.
doi:10.1093/mnras/stw2759
- Moretti, A., Pagani, C., Cusumano, G., et al. 2009, *A&A*, 493, 501. doi:10.1051/0004-6361:200811197
- Nasa High Energy Astrophysics Science Archive Research Center (Heasarc) 2014, *Astrophysics Source Code Library*. ascl:1408.004
- Navarro, J. F., Frenk, C. S., & White, S. D. M. 1997, *ApJ*, 490, 493. doi:10.1086/304888
- Neronov, A., Malyshev, D., & Eckert, D. 2016, *PhRvD*, 94, 123504. doi:10.1103/PhysRevD.94.123504
- Neronov, A. & Malyshev, D. 2016, *PhRvD*, 93, 063518.
doi:10.1103/PhysRevD.93.063518
- Nesti, F. & Salucci, P. 2013, *JCAP*, 2013, 016.
doi:10.1088/1475-7516/2013/07/016
- Ng, K. C. Y., Horiuchi, S., Gaskins, J. M., et al. 2015, *PhRvD*, 92, 043503. doi:10.1103/PhysRevD.92.043503
- Ng, K. C. Y., Roach, B. M., Perez, K., et al. 2019, *PhRvD*, 99, 083005. doi:10.1103/PhysRevD.99.083005
- Pagani, C., Morris, D. C., Racusin, J., et al. 2007, *Proc. SPIE*, 6686, 668609. doi:10.1117/12.734398
- Pal, P. B. & Wolfenstein, L. 1982, *PhRvD*, 25, 766.
doi:10.1103/PhysRevD.25.766
- Pedregosa, F., Varoquaux, G., Gramfort, A., et al. 2012, *arXiv:1201.0490*
- Perez, K., Ng, K. C. Y., Beacom, J. F., et al. 2017, *PhRvD*, 95, 123002. doi:10.1103/PhysRevD.95.123002
- Roach, B. M., Ng, K. C. Y., Perez, K., et al. 2020, *PhRvD*, 101, 103011. doi:10.1103/PhysRevD.101.103011
- Roach, B. M., Rossland, S., Ng, K. C. Y., et al. 2022, *arXiv:2207.04572*
- Ruchayskiy, O., Boyarsky, A., Iakubovskiy, D., et al. 2016, *MNRAS*, 460, 1390. doi:10.1093/mnras/stw1026
- Schneider, A. 2015, *MNRAS*, 451, 3117.
doi:10.1093/mnras/stv1169
- Serpico, P. D. & Raffelt, G. G. 2005, *PhRvD*, 71, 127301.
doi:10.1103/PhysRevD.71.127301
- Sicilian, D., Cappelluti, N., Bulbul, E., et al. 2020, *ApJ*, 905, 146. doi:10.3847/1538-4357/abbee9
- Silich, E. M., Jahoda, K., Angelini, L., et al. 2021, *ApJ*, 916, 2. doi:10.3847/1538-4357/ac043b
- Tamura, T., Iizuka, R., Maeda, Y., et al. 2015, *PASJ*, 67, 23. doi:10.1093/pasj/psu156
- The pandas development team 2020, *Zenodo*.
doi:10.5281/zenodo.3509134
- Urban, O., Werner, N., Allen, S. W., et al. 2015, *MNRAS*, 451, 2447. doi:10.1093/mnras/stv1142
- van der Walt, S., Colbert, S. C., & Varoquaux, G. 2011, *Computing in Science and Engineering*, 13, 22.
doi:10.1109/MCSE.2011.37
- Venumadhav, T., Cyr-Racine, F.-Y., Abazajian, K. N., et al. 2016, *PhRvD*, 94, 043515.
doi:10.1103/PhysRevD.94.043515
- Vikhlinin, A., McNamara, B. R., Forman, W., et al. 1998, *ApJ*, 502, 558. doi:10.1086/305951
- Wik, D. R., Hornstrup, A., Molendi, S., et al. 2014, *ApJ*, 792, 48. doi:10.1088/0004-637X/792/1/48